Published in "Bulletin of the Seismological Society of America 106(5): 2023–2036, 2016" which should be cited to refer to this work.

# Optimizing Event Detection and Location in Low-Seismicity Zones: Case Study from Western Switzerland

by Naomi Vouillamoz,* Gilles Hillel Wust-Bloch, Martinus Abednego, and Jon Mosar

**Abstract** Obtaining robust event catalogs in regions of low seismicity can be time-consuming, because quality events are less frequent and sensor coverage is generally sparse. Optimizing event detection and location in such regions is all the more crucial because these areas tend to host a higher density of sensitive infrastructures. The methodology proposed consists of reprocessing existing data recorded by a permanent network and boosting the final catalog resolution by temporarily deploying portable sparse mini-arrays in the target area. Sonogram analysis is applied on both existing and new datasets to detect waveforms barely emerging from the background noise. A visual interactive event analysis module is used to test for phase picking, event association, waveform cross correlation, and location ambiguities. It also estimates back azimuth and slowness when sparse array data are available. The method is applied to a low-seismicity region in the western Swiss Molasse basin where two sparse mini-arrays were temporarily deployed. The detection of earthquakes is improved by a factor of 9 when reprocessing four yrs (2009–2013) of available data recorded by two accelerometers and one broadband station in a 2500 $km^2$ target area. Magnitude estimations are empirically calibrated over four magnitude units, down to $-1.7$ $M_L$, lowering the existing catalog completeness by close to one magnitude unit. After validating picking and location accuracies with a standard residual-based scheme, 174 newly detected events are relocated, illuminating zones of previously undetected microseismic activity.

*Online Material:* Earthquake catalog FRICAT.

## Introduction

In regions of low-seismicity rate, catalog size and quality are inferior due to lower sensor density and longer recurrence time of events. Studies of weak microseismicity are also crucial because these regions are generally selected to host sensitive infrastructures and are the target of increasing induced seismicity operations (e.g., Deichmann and Giardini, 2009; Kraft *et al.*, 2009; Edwards *et al.*, 2015). The unfavorable signal-to-noise ratio (SNR) conditions in these regions make it even more challenging to meet short deadlines for seismic-hazard assessment. This article investigates the capabilities of nanoseismic monitoring (Wust-Bloch and Joswig, 2006; Joswig, 2008; Sick *et al.*, 2012) to optimize earthquake detection and location for the low-seismicity western Swiss Molasse basin. The nanoseismic monitoring approach is used to reprocess data recorded by three local stations operated by the Swiss Seismological Service (SED) in the target area. Between 2009 and 2013, 271 new events are added to 34 events included in the earthquake catalog of Switzerland (ECOS; Fäh *et al.*, 2003; see Fäh *et al.*, 2011, in Data and Resources) in the same period and area. The nanoseismic monitoring interactive location scheme HypoLine (Joswig, 2008) is then validated with NonLinLoc (NLL; Lomax *et al.*, 2000, 2009), a standard location algorithm based on residuals. Results show that the analyst-guided location scheme of nanoseismic monitoring is more robust than NLL when investigating microseismic datasets with few low-SNR phase onsets, because displaying all constraints in real time allows for superior ambiguity resolution (Eisermann *et al.*, 2015).

The western Swiss Molasse basin is an area of low-seismic activity, for which only four $M_w$ 4.0–4.5 events were reported in the original ECOS (period 1600–2002; Fäh *et al.*, 2003). Between 1987 and 1999, three series of earthquakes, one of them reaching local magnitude $M_L$ 4.3, occurred in the sedimentary cover near the city of Fribourg (Deichmann

*Now at Institute for Geophysics, University of Stuttgart, Azenbergstrasse 16, 70174 Stuttgart, Germany; naomi.vouillamoz@geophys.uni-stuttgart.de.

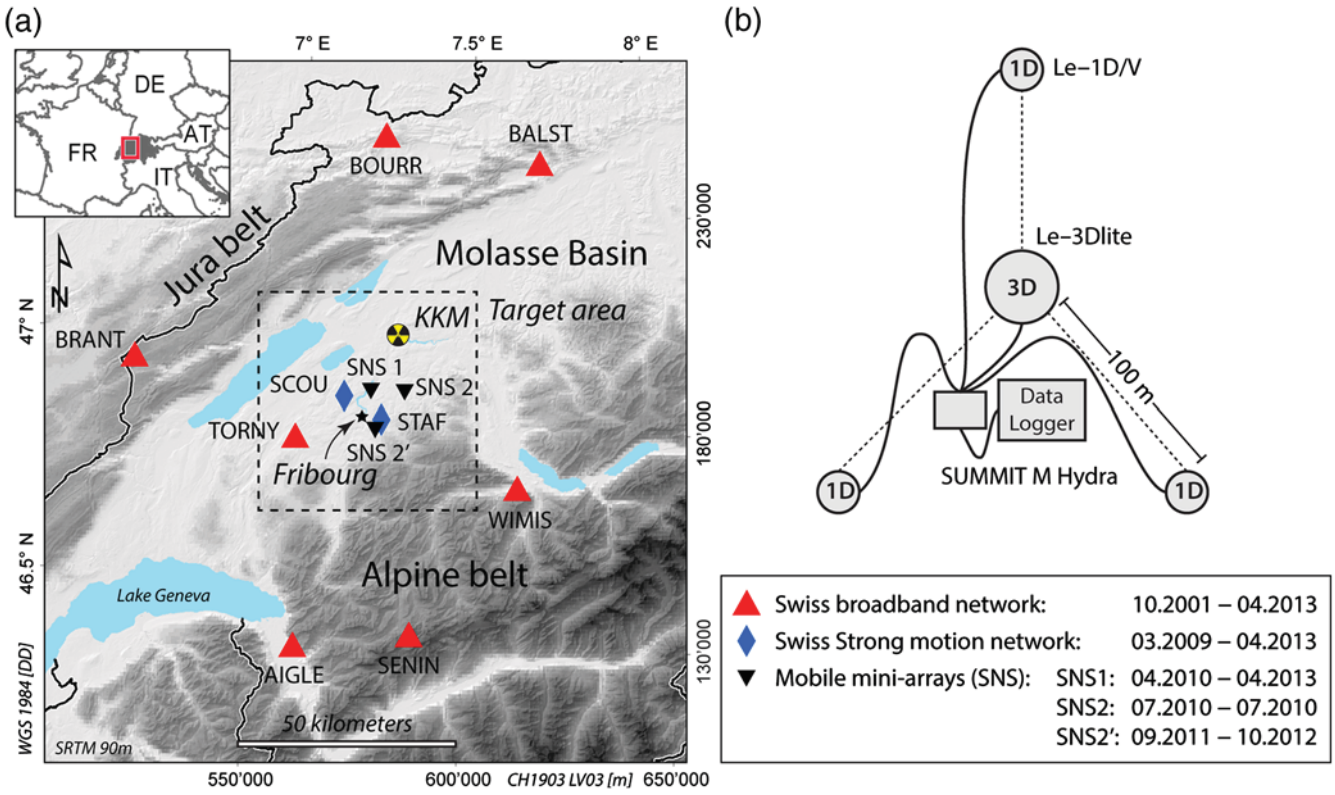


**Figure 1.** (a) Swiss Seismological Service (SED) broadband stations (triangles), SED accelerometers (diamonds), and mini-arrays (reversed triangles) used in this study. Kernkraftwerk Mühleberg (KKM) shows the location of the Mühleberg nuclear power plant in the target zone. Legend at the bottom right indicates periods of investigated continuous records of SED data and periods of mini-array operation in the target area. (b) Scheme of a sparse array (Seismic Navigating System [SNS]). The color version of this figure is available only in the electronic edition.

*et al.*, 2000; Kastrup *et al.*, 2007) along a north–south alignment. Because these events did not correlate with the main tectonic features of the area, it was suggested that they may be associated with a crustal structure capable of generating an earthquake in the magnitude **M** 6 range (Kastrup *et al.*, 2007). The present study was initially undertaken to provide sufficient microseismic data to assess the vulnerability of the Mühleberg nuclear power plant (Fig. 1).

## Data

The Swiss national network operated by the SED prior to 2013 is sparse in the western Swiss Molasse basin region (Diehl *et al.*, 2014) (Fig. 1). One broadband station (TORNY) and two accelerometers (STAF and SCOU) operate within the target area (Deichmann *et al.*, 2010; Clinton *et al.*, 2011). The magnitude of completeness for that area during the 1983–2008 period is around $M_L$ 2.0 (Nanjo *et al.*, 2010; Kraft *et al.*, 2013). Our new FRICAT catalog integrates continuous records of TORNY, STAF, and SCOU (March 2009–April 2013) that were reprocessed by sonogram analysis and a new dataset recorded by two portable mini-arrays deployed near Fribourg (March 2010–April 2013; Fig. 1). Each mini-array is designed as a Seismic Navigating System (SNS; Wust-Bloch and Joswig, 2006; Joswig, 2008) consisting of three vertical short-period sensors arranged in a tripartite layout around a central three-axis short-period sensor. SNSs were deployed as close as possible to potential seismogenic sources delineated by the ECOS (Fäh *et al.*, 2003; see Fäh *et al.*, 2011, in Data and Resources). The geometry and aperture (±100 m) of SNS was guided by local logistical constraints. The sensors (Lennartz 1D/V and 3Dlite) were buried at 50 cm depth and coupled with the Quaternary formations by fine gravels and sand. Data were sampled in a continuous mode at 250 Hz by SUMMIT-Hydra series data loggers and accessed remotely in quasi-real time. The high-ambient seismic noise level in the target area (root mean square ground velocities around 139 nm/s in 1–10 Hz; Kraft *et al.*, 2013) and the deployment of the mini-arrays on Quaternary sediments resulted in low-SNR records (Fig. 2).

Seismic data of six additional SED broadband stations were used in a second phase to improve earthquake locations and local magnitude evaluation (Fig. 1). To identify weaker events that were previously undetected before March 2009 (first availability of SCOU and STAF records in SED archives), we reprocessed available continuous records of the six SED broadband stations 48 hrs before and after each ECOS event located in the target area. The main parameters of the stations used in this study are described in Table 1. Figure 2 shows the time distribution of the seismic data processed by sonogram screening.

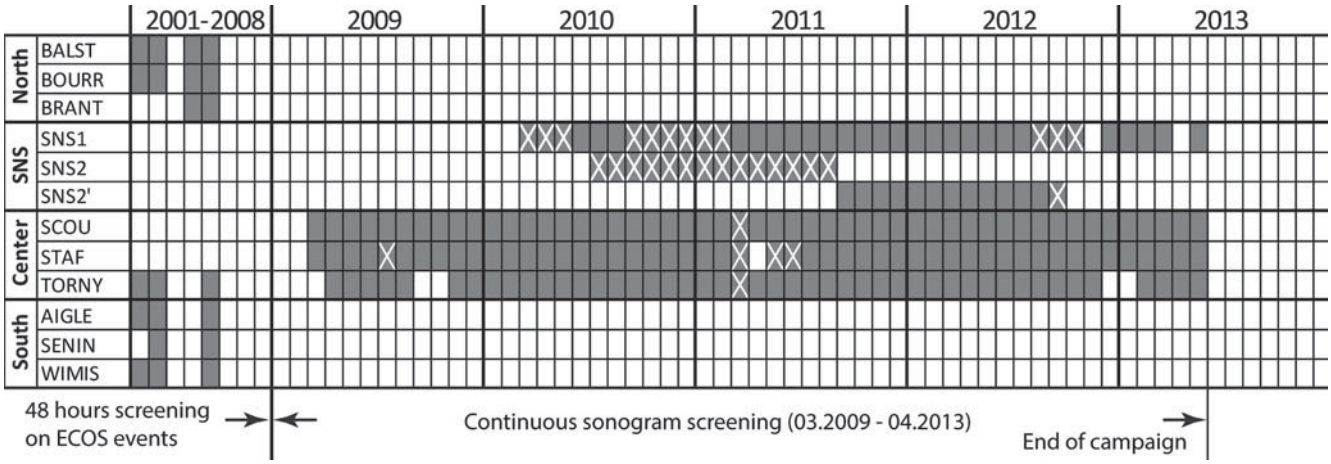


**Figure 2.** Time distribution of seismic records processed by sonogram screening (solid fill). Before March 2009, time windows of 48 hrs before and after each event reported by the earthquake catalog of Switzerland (ECOS) are screened on available broadband records to detect potential associated events. Between March 2009 and April 2013, data recorded by stations SCOU, STAF, and TORNY, as well as SNS data are continuously screened by sonograms. Crosses indicate measurements with high level of background noise.

## Methodology

The methodology followed here consists of optimizing nanoseismic monitoring (Wust-Bloch and Joswig, 2006; Joswig, 2008; Sick *et al.*, 2012, 2015) and validating its picking and location scheme with standard residual-based approaches. Nanoseismic monitoring was originally developed to characterize extremely weak seismicity ($M_L \geq -3.0$) at short slant distances ($10–10^4$ m; Wust-Bloch and Joswig, 2006). It is supported by a real-time multiparameter visualization approach that integrates power-density matrix signal processing with dual (array and network) mode location schemes that enable earthquake detection and location down to the noise threshold. First, signals barely emerging from the background noise threshold are identified by sonogram analysis, a type of spectrogram with dynamic frequency-dependent noise adaptation (Joswig, 1990, 1995; Sick *et al.*, 2012). Then, waveforms are evaluated interactively for initial signal coherence, back azimuth, and slowness to provide an optimized graphical hypocentral solution, simultaneously processing data in network and array mode (Joswig, 2008).

Table 1
Station Network

| Code | Station | Latitude (°) | Longitude (°) | Elevation (m) | Channel | Sampling Rate (Hz) | Gain (nm/s/count) | Calper (s) |
|---|---|---|---|---|---|---|---|---|
| BALST | Balsthal | 47.33578 | 7.69498 | 908 | HHZ/N/E | 120 | $5.07 \times 10^{-2}$ | 0.2 |
| BOURR | Bourrignon | 47.39377 | 7.23018 | 860 | HHZ/N/E | 120 | $5.07 \times 10^{-2}$ | 0.2 |
| BRANT | Les Verrières | 46.93801 | 6.47298 | 1145 | HHZ/N/E | 120 | $5.31 \times 10^{-2}$ | 0.2 |
| SCOU | Cournillens | 46.85400 | 7.10370 | 600 | HGZ/N/E | 250 | $2.45 \times 10^{3}$ | 6.283 |
| STAF | Tafers | 46.80520 | 7.21610 | 650 | HGZ/N/E | 250 | $2.45 \times 10^{3}$ | 6.283 |
| TORNY | Torny | 46.77365 | 6.95862 | 758 | HHZ/N/E | 120 | $5.07 \times 10^{-2}$ | 0.2 |
| AIGLE | Aigle | 46.34161 | 6.95336 | 800 | HHZ/N/E | 120 | $5.07 \times 10^{-2}$ | 0.2 |
| SENIN | Lac Selin | 46.36335 | 7.29930 | 2035 | HHZ/N/E | 120 | $5.07 \times 10^{-2}$ | 0.2 |
| WIMIS | Winmis | 46.66488 | 7.62418 | 770 | HHZ/N/E | 120 | $5.07 \times 10^{-2}$ | 0.2 |
| SNS1-C | Allenlüften | 46.86340 | 7.18509 | 620 | SHZ/N/E | 250 | $3.98 \times 10^{-4}$ | 1 |
| SNS1-E | Allenlüften | 46.86400 | 7.18675 | 618 | HHZ | 250 | | |
| SNS1-N | Allenlüften | 46.86415 | 7.18591 | 618 | HHZ | 250 | | |
| SNS1-W | Allenlüften | 46.86384 | 7.18415 | 620 | HHZ | 250 | | |
| SNS2-C | Flamatt | 46.86334 | 7.28615 | 686 | SHZ/N/E | 250 | $3.98 \times 10^{-4}$ | 1 |
| SNS2-E | Flamatt | 46.86344 | 7.28747 | 686 | HHZ | 250 | | |
| SNS2-N | Flamatt | 46.86280 | 7.28607 | 694 | HHZ | 250 | | |
| SNS2-W | Flamatt | 46.86351 | 7.28491 | 687 | HHZ | 250 | | |
| SNS2'-C | Fromatt | 46.78585 | 7.19880 | 716 | SHZ/N/E | 250 | $3.98 \times 10^{-4}$ | 1 |
| SNS2'-E | Fromatt | 46.78525 | 7.19942 | 718 | HHZ | 250 | | |
| SNS2'-N | Fromatt | 46.78638 | 7.19972 | 713 | HHZ | 250 | | |
| SNS2'-W | Fromatt | 46.78630 | 7.19794 | 719 | HHZ | 250 | | |

Station list with receivers' main parameters. Channel instrument code: HH, high broadband—high-gain seismometer; HG, high broadband—accelerometer; SH, short-period seismometer; Z/N/E, orientation code—vertical/north–south/east–west, gain and calper, GSE-2 amplification factor and calibration period.

## Lowering Detection Threshold

Because conventional automatic short-term average/long-term average-based detectors (Withers *et al.*, 1998; Trnkoczy, 2012) are not suited to the substandard SNR conditions expected for the target events, datasets are screened by sonogram analysis (Sick *et al.*, 2012). This signal inspection scheme computes a power spectral density matrix which is processed with autoadaptive noise muting and prewhitening and then binned logarithmically for frequency and amplitude (Joswig, 1990, 1995; Sick *et al.*, 2012). Event detection and type identification are carried out on continuous sonograms, displayed simultaneously for the selected SED stations and SNS on a common timeline scale (NanoseismicSuite package by Sick *et al.*, 2012). A typical sonogram pattern for an earthquake maximizes signal onset and enhances changes in distribution of signal energy as a function of time and frequency. Sonogram pattern similarity facilitates the detection of events in low-SNR conditions on single or multiple traces. This is illustrated by a series of earthquake sequences recorded in October 2001 by SED broadband stations BALST, TORNY, AIGLE, and WIMIS (Fig. 3). Only the initial and last events are included in the ECOS (Fäh *et al.*, 2003). Sonogram analysis of continuous data between 11–12 October 2001 detects an additional eight low-magnitude events ($M_L < 1$). *P* and *S* phases are clearly identified at BALST and are consequently recognizable at others: the semicircular pattern displayed by the sonograms of stronger events is easily recognizable for weaker events. The ability of sonogram analysis to enhance low-SNR signals is best observed when compared with standard vertical traces (Fig. 4a). East-horizontal traces of the *S*-phase onsets display a high-waveform similarity that suggests shared source properties (Fig. 4b). The sonogram pattern recognition analysis resulted in the identification of 282 previously undetected events (86% of the complete 2001–2013 dataset). They include 146 new earthquakes and 136 associated aftershocks.

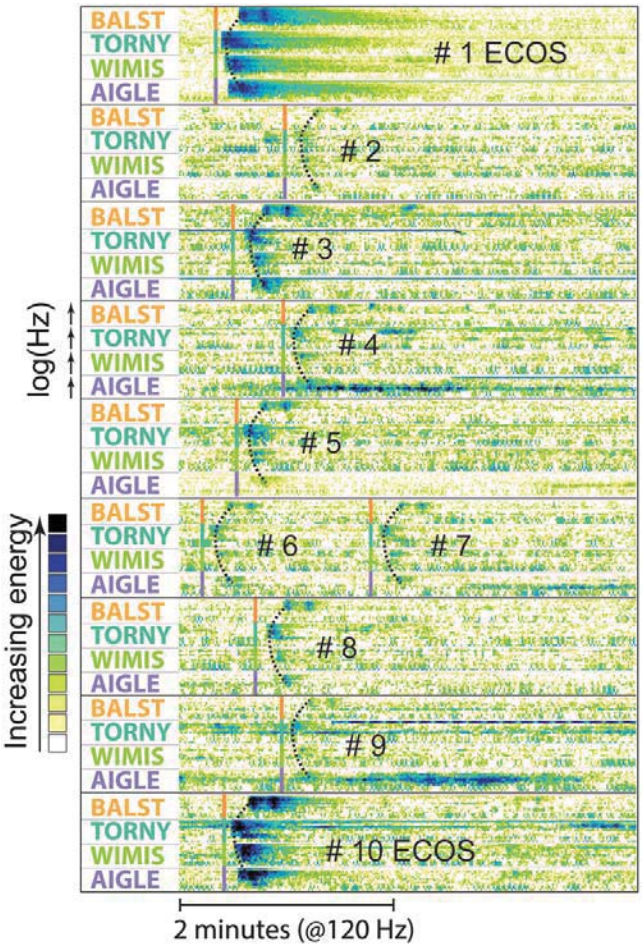


**Figure 3.** Sequence of weak events recorded on 11–12 October 2001. Event numbers 1 and 10 are reported in ECOS (Fäh *et al.*, 2003). The similarity of sonogram displayed at four nearby broadband stations (AIGLE, BALST, TORNY, and WIMIS) help identify eight weaker events previously undetected. See Figure 4 for date and origin time of the individual events. The color version of this figure is available only in the electronic edition.

## Optimizing Event Location

The analysis and location of low-magnitude events simultaneously recorded by sparse networks and by array stations are not trivial issues. HypoLine software (Joswig, 2008) was selected because it supports event location, simultaneously in network and in array mode. Unlike standard residual-based location algorithms, HypoLine presents a visual display of multiple location parameters, updated in real time, which guide the analyst in selecting a solution (Fig. 5a,b). Once phase arrivals are picked (on sonograms or standard waveforms) and a velocity model selected, HypoLine displays the *S*–*P* travel-time ($t_S$–$t_P$) curves at a given depth in addition to the equal differential time (EDT) hyperboloids derived for each pair of $t_P$–$t_P$ onset times (Joswig, 2008). Variable phase onsets and velocity models can be simulated endlessly in real time, and the most plausible hypocentral solution is selected by the analyst as the zone with the highest concentration of intersecting constraints (Fig. 5a). This real-time graphic display simulates all location constraints in a single window, allowing for unlimited testing of location parameters. It supports a jackknifing-like approach that displays potential outliers and shows how they may bias hypocentral solutions. HypoLine provides robust solutions, especially when data are sparse, onsets weak, and the potential for ambiguities high. HypoLine software supports layered $V_P$ velocity models with constant $V_P/V_S$ ratio. In this study, the SED 3D $V_P$ model (Husen *et al.*, 2003) was customized for the Fribourg region with a $V_P/V_S$ ratio of 1.78, which best suits the sedimentary subsurface (Table 2). In array mode, vertical traces are cross-correlated over the array, and back azimuths are retrieved by jackknifing (Fig. 5b). Back-azimuth predictions are then intersected with $t_S$–$t_P$ 3D surfaces and EDT hyperboloids to locate weak events (see Fig. 5a), and slowness is used to discriminate nonseismic events. A cross-correlation-based master-event associator supports interactive slave-event relocation, in which autoadaptive scaling helps to visually

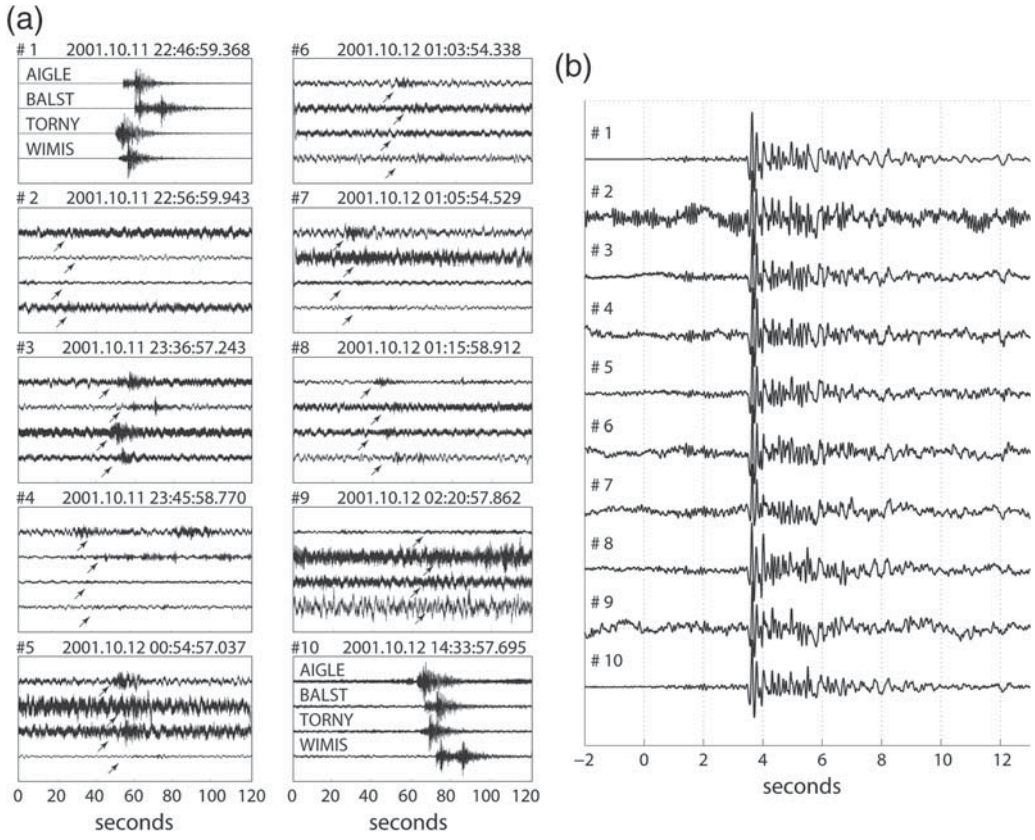


**Figure 4.** (a) The seismograms of the 10 events displayed in Figure 3 (vertical traces, ground velocity, high-pass filtered above 1 Hz) at stations AIGLE, BALST, TORNY, and WIMIS are shown for comparison. Small arrows indicate phase arrivals detected in Figure 3. (b) The strong waveform similarity observed on the east-horizontal traces (ground velocity, 1–30 Hz) at station TORNY suggests shared source location and features.

evaluate a best fit between related phases (Fig. 5c). Subsequent pairs of relative *P* onsets determine misfit vectors (spatial offset between the EDT hyperboloids of the master and the slave events) linked to the master-event hypocenter location. The normalized sum of the mislocation vectors gives an approximated solution for the relocated event, and the spread of the mislocation vectors displays the goodness and stability of the collocation (Häge *et al.*, 2013).

### Benchmarking Interactive and Residual-Based Location Schemes

HypoLine does not provide a standard evaluation scheme for location uncertainty (Joswig, 2008). Thus, it is benchmarked by comparing its epicentral solutions with those computed by a residual-based location scheme. The analysis uses as a baseline the 45 events of the ECOS catalog in the target area (2001–2013; $0.4 < M_L < 2.4$). The standard location procedure followed for the ECOS includes probabilistic onset picking following Diehl *et al.* (2009) with Seismic Network Analysis Program (SNAP; Baer, 1992) and location with NLL (Lomax *et al.*, 2009) using a 3D velocity model (Husen *et al.*, 2003). NLL is used assuming Gaussian errors for phase onset time and for travel-time calculation. Onset uncertainties are defined in SNAP according to five *P*-phase ranking classes (I, 0.025 s; II, 0.05 s; III, 0.1 s; IV, 0.2 s; V, 0.4 s). However, manual location rejects phase onsets with uncertainties above 0.2 s (N. Deichmann, personal comm., June 2012). Two additional catalogs are designed for benchmarking purposes; both use HypoLine-based phase pickings. These pickings are first exported in SNAP, where onset uncertainties are defined using ECOS *P*-phase ranking classes. Then, the 45 events are located with NLL and the 3D velocity model by Husen *et al.* (2003) according to two criteria: (1) the NLL-A catalog relocates only with high-quality phase onsets (classes I–III), thus, NLL-A solutions are equivalent to standard ECOS manual locations; (2) the NLL-B catalog uses all phase pickings (classes I–V), including high-uncertainty arrivals. The HYPOLINE catalog includes epicentral solutions of the 45 events estimated interactively by HypoLine, using the customized 1D velocity model based on Husen *et al.* (2003). Given the simplicity of the 3D velocity model (Husen *et al.*, 2003) used by NLL for the Fribourg region, we expect that phase picking will have a much more important effect on locations than velocity models.

Variations in epicentral solutions for ECOS–HYPOLINE (Fig. 6a), ECOS–NLL-A (Fig. 6b), and HYPOLINE–NLL-A (Fig. 6c) are minimal as indicated by low standard deviations ($\sigma$). The match between locations, which is better at the center of the target zone, may be related to the proximity and

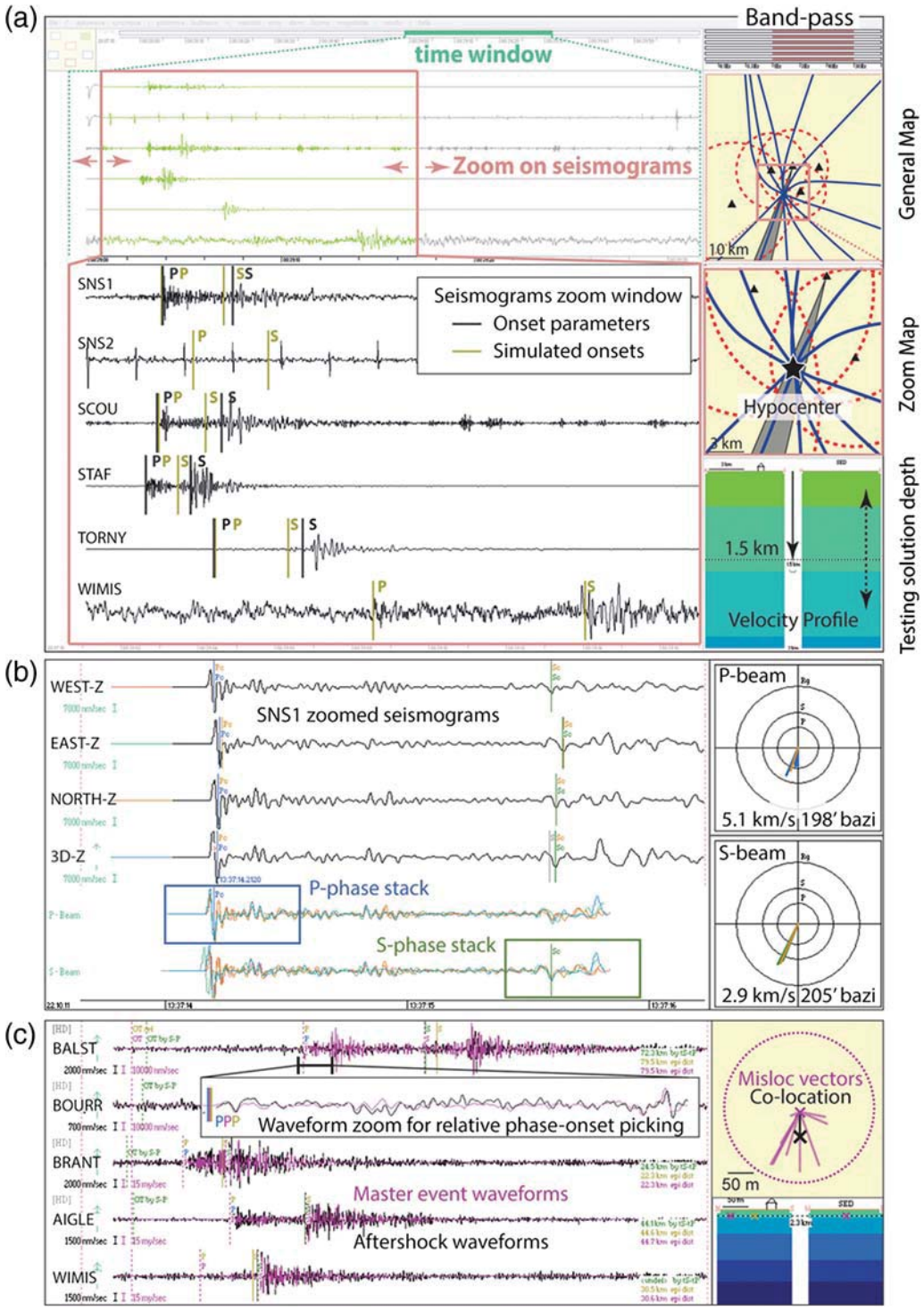


**Figure 5.** (a) Location of 28 July 2010 event ($M_L$ 0.8) by HypoLine (network mode) whereby picking of *P* and *S* onsets derive real-time $t_S$–$t_P$ surfaces (dotted circles) and $t_P$–$t_P$ equal differential time (EDT) hyperboloids (bold lines) in maps at right. Array processing (in array mode) of SNS1 records derives a back-azimuth beam of about 200° in maps (shaded triangle). The hypocenter is found in the zoom map by looking for the highest concentration of intersecting location constraints, by selecting an adequate velocity profile, and by testing it through the depth profile (bottom right). Picking a solution in the map will display simulated phase onsets on seismograms in real time, supporting a trial-and-error jackknifing approach to location. (b) Array mode (event of 22 October 2011, $M_L$ 2.1) where time offsets of phase onsets of a single SNS are used to estimate apparent velocity and back azimuth. In this case, the *P* and *S* phases show a similar back azimuth at 200° and *P*- and *S*-phase velocities of 5.1 and 2.9 km/s, respectively (circle plots at right). (c) Master-event relocation mode showing the misfit vectors between the EDT hyperboloids derived from relative *P*-onsets of a master event and a slave event (ECOS 11 October 2001 22:48 and 23:37 UTC). The normalized sum of the mislocation vectors indicates a collocation offset by 50 m to the south with good constraints (low-angle spread of the mislocation vectors). The color version of this figure is available only in the electronic edition.

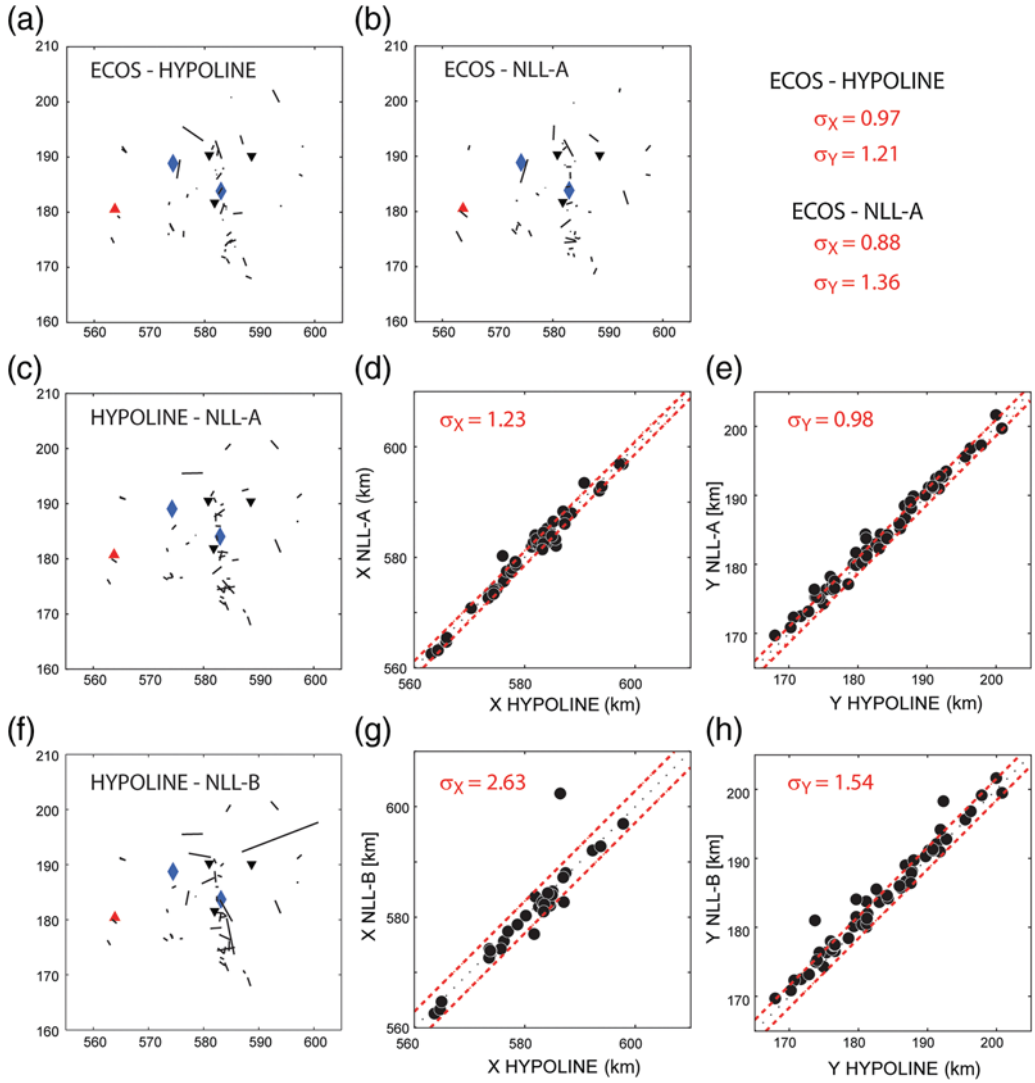


**Figure 6.** Variability in epicentral locations for four catalogs: ECOS, HYPOLINE, NLL-A, and NLL-B. Coordinates are CH1903 projections (km), and symbols indicate the station network (see legend on Fig. 1). (a,b) Comparison of ECOS with HYPOLINE and NLL-A in map views. (c–e) Comparison of (c) HYPOLINE and NLL-A catalogs in map view, (d) easting $X$–$X$, and (e) northing $Y$–$Y$ plots. (f–h) Comparison of (f) HYPOLINE and NLL-B catalogs in map view, (g) $X$–$X$, and (h) $Y$–$Y$ plots (see discussion in the Benchmarking Interactive and Residual-Based Location Schemes section). The color version of this figure is available only in the electronic edition.

geometry of the TORNY, STAF, and SCOU stations (Fig. 1a). Standard deviations in $X$ and $Y$ for HYPOLINE–NLL-A (Fig. 6d,e) are below 1.23 km and thus match epicentral uncertainties of high-quality events (Deichmann *et al.*, 2010). Comparing solutions for HYPOLINE–NLL-A (Fig. 6c–e) suggests that, with identical phase pickings, location variations are negligible whether solutions are computed by NLL algorithms or selected manually by HypoLine. Finally, HYPOLINE epicentral solutions are compared to those of NLL-B (Fig. 6f–h), in which low-quality phase pickings are also included. The impact of these low-quality arrivals on the residual-based solutions of NLL-B was quantified (Vouillamoz, 2015). They cause larger epicentral offsets (Fig. 6f) and higher standard deviations between $X$ and $Y$ values in HYPOLINE and NLL-B catalogs (Fig. 6g,h). Therefore, it can be concluded that HypoLine facilitates identifying and culling bad data when processing low-SNR events: erroneous parameters, which are unambiguously recognized as not matching the

Table 2
Fribourg Velocity Model

| Thickness (km) | $P$ Velocity (km/s) | $V_P/V_S$ |
|---|---|---|
| 0.6 | 4.5 | 1.78 |
| 1.1 | 4.9 | |
| 1.1 | 5.6 | |
| 4.9 | 5.9 | |
| 8.2 | 6 | |
| 6.7 | 6.1 | |
| 8.9 | 7 | |
| Half-space | 8.2 | |

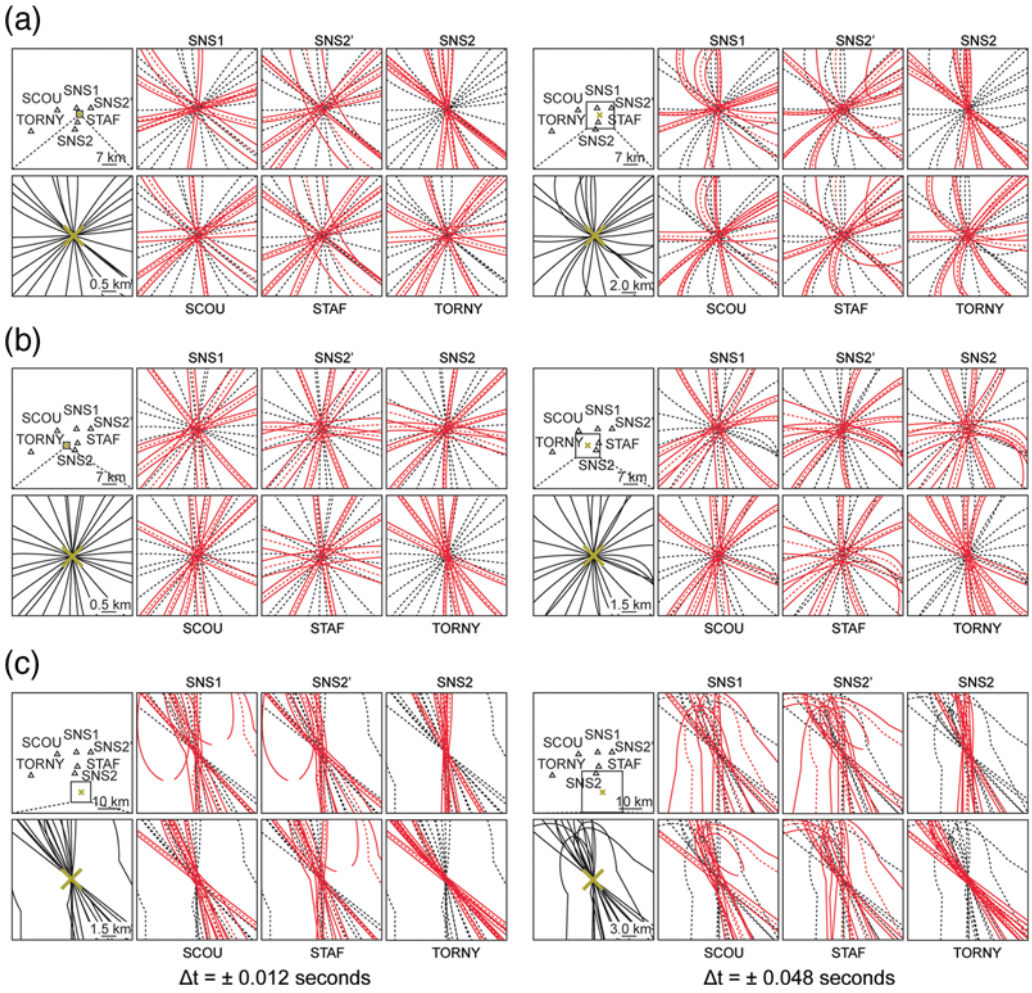


**Figure 7.** Three synthetic locations representative of the target area seismicity are analyzed by HypoLine software: (a) Fribourg lineament: 46.84° latitude, 7.22° longitude, 3.5 km depth; (b) Fribourg city: 46.80° latitude, 7.15° longitude, 3.5 km depth; and (c) St-Sylvester region: 46.71° latitude, 7.24° longitude, 2.5 km depth. Each subpanel includes in the two subplots at left a general map with scaling, stations and synthetic event location as well as the sets of EDT hyperboloids that result from synthetic *P* onsets at the nearest stations SCOU, STAF, TORNY, and arrays SNS1 and SNS2/SNS2' (central sensors). At each station, the synthetic *P* is advanced or delayed by ±3 samples (left panel) and ±12 samples (right panel) to quantify location change. The spatial evolution of the EDT hyperboloids (bold lines) enables monitoring of the uncertainties on the location solution that are caused by a first-order (±0.012 s) or a third-order (±0.048 s) quality phase onset as considered by the SED at the respective stations. The color version of this figure is available only in the electronic edition.

global solution, are routinely discarded from the final solution. This is not an option for standard residual-based location for which the inclusion of low-quality data adversely affects location accuracy and dataset robustness. In conclusion, we see that when fed identical high-quality data, analyst-based and residual-based location approaches perform equally well. However, as soon as the waveform quality or amplitude drops, HypoLine has unmatched detection power when no prior information is available. It is able to screen out the effects of potential outliers, and it provides robust locations with minimal data.

### Sensitivity Analysis for Epicentral Locations by HypoLine

Three case studies were designed within the target area to assess the sensitivity of epicentral location by HypoLine to phase picking (Fig. 7). The analysis uses the sets of EDT hyperboloids computed by *P* onsets picked at the five nearest stations (SCOU, STAF, TORNY, SNS1, and SNS2/SNS2'; central three-axis sensors are selected for SNS). Phase onset variability of 6 and 12 samples (at 250 Hz) are tested, corresponding to ECOS uncertainty classes I and III. The Fribourg Lineament case (Fig. 7a) shows that uncertainties in phase onsets registered at stations STAF and SNS2' lead to important east–west variability that might explain part of the east–west lateral spread observed in the final locations. The Fribourg city case (Fig. 7b) indicates that the spatial layout of the five stations around the target is optimal, resulting in stable location constraint. The St-Sylvester case (Fig. 7c) shows that, because events are located out of the stations' network, hyperbolae intersect at very low angles, resulting in unstable solutions and larger uncertainties that are strongly biased in

the north–south direction (note the larger scaling in Fig. 7c). This sensitivity analysis corroborates previous observations (Fig. 6) and confirms that location bias is minimal at the center of the target zone and stronger at the edge of the target zone, affected by the station geometry.

## Integrated Catalog (FRICAT)

The interactive evaluation of events by HypoLine requires a rigorous procedure. Phase onsets are picked using a probabilistic function for time arrivals (Diehl *et al.*, 2009), and particular attention is devoted to selecting uniform time windows and amplitude scaling settings when defining the phase onsets. Waveforms are band-pass filtered between 1 and 30 Hz. Data with very low SNR are additionally low-pass filtered at 10 Hz. Hypocentral solutions are computed only for high-SNR events recorded at more than five nearby stations. Only the epicenter solution is estimated when less than five stations are available. Finally, the events are sorted into four classes.

- Class A (50% of final 2001–2013 dataset): hypocentral/epicentral solution is computed by a minimum of five sets of high-SNR location constraints ($t_P$–$t_P$ EDT hyperboloids, $t_S$–$t_P$ surfaces, and/or back-azimuth beams). Location constraints converge to a consistent solution, resulting in epicentral uncertainties below 2 km.
- Class B (20% of final 2001–2013 dataset): epicentral solution is computed by less than five sets of high-SNR location constraints. Resulting epicentral uncertainties are between 2 and 5 km.
- Class C (30% of final 2001–2013 dataset): event is only recorded by stations STAF, SCOU, and/or TORNY. Both *P* and *S* phases can be picked. The event is not located but used for the magnitude catalog because *S*–*P* travel-time differences are available.
- Class XC (cross correlated, 45% of FRICAT events): event that belongs to an earthquake sequence. It is collocated with a class A and class B master events or simply associated to a class C master event using cross-correlation options in HypoLine (Fig. 5c) (see 54 detected earthquake sequences with 198 events in the Ⓔ electronic supplement to this article).

Between October 2001 and April 2013, the ECOS catalog located 45 events in the target area. Reprocessing the same dataset by sonogram analysis resulted in the increased detection of 282 new events. For the period 2009–2013 (during which two new accelerometers SCOU and STAF are deployed in the target area), the full data were continuously screened by sonogram. The sonogram analysis detected 272 new events, consequently increasing the original number of ECOS events (34) by a factor of 9 (304/34). Because 136 of the new detections are associated with earthquake sequences, a portion of these events could have been detected through standard seismogram-based matched filter or matched signal detector (e.g., Gibbons and Ringdal, 2006; Schaff and Waldhauser, 2010; Plenkers *et al.*, 2013). Therefore, the remaining 146 unmatched events (~50% of the 2009–2013 sonogram events) represent the true gain by sonogram screening. Being self-adaptive (Joswig, 1995), sonograms do not require prior information, and event detection can be carried out without an initial template, which is not the case for standard template matching techniques. Automated sonogram-based detection algorithms are presently being tested (Sick *et al.*, 2015).

The 45 ECOS events and the 282 newly detected events are merged into a joint uniform database: the FRICAT catalog with a total of 327 events (see Ⓔ electronic supplement to this article). About 60% of the newly detected events between 2001 and 2013 could be located by HypoLine (174 events, 65 unmatched events, and 109 correlated events, Fig. 8a). A good fit is observed between epicentral solutions of FRICAT class A events and mapped subsurface tectonic features (Interoil, 2010; Meier, 2010). This is particularly striking along the Fribourg and St-Sylvester structures, a series of north–south fault zones in the Mesozoic cover, east of the city of Fribourg (Fig. 8b). The collocation of earthquake sequences also shows a preferred north–south orientation (i.e., Fig. 5c), corroborating the north–south fault-plane solutions determined for the 1987, 1995, and 1999 sequences (Kastrup *et al.*, 2007). Most hypocentral solutions are shallow (<4.5 km). Only a few events that were recorded before SCOU and STAF accelerometers started operating in 2009 are located in the basement. Because the depth of these events is constrained by phase arrivals recorded at broadband stations where the near-surface velocity structure is different from the one observed within the Molasse basin, the resulting depth may be overestimated (Kastrup *et al.*, 2007). Therefore, the local seismicity seems to be generated by fault zones within the sedimentary cover and no evidence exists, which can associate the observed seismicity with deeper crustal structures. Given their performance in low-SNR conditions, the mini-arrays provided new, robust constraints on the weak seismicity generated below the city of Fribourg, where no seismic subsurface data are available (Fig. 8c). These results illustrate the potential of the nanoseismic monitoring approach in characterizing weak seismicity in areas where network coverage is suboptimal.

## Magnitude Catalog

The low energy of FRICAT events resulted in signals recorded mostly at short hypocentral distances. Consequently, 47% of the amplitude readings are picked at recording distances below 10 km and 66% below 20 km (Fig. 9a). These data project into the uncalibrated distance range of regional magnitude relationships, such as SED in Switzerland (Kradolfer, 1984) and Baden-Württemberg Seismological Service (LED) in southwestern Germany (Stange, 2006) (Fig. 9b). Therefore, an adequate magnitude relationship must be selected. The Swiss magnitude relationship by Kradolfer (1984) was recently recalibrated for distance below 20 km using data from ~2700 events (Edwards *et al.*, 2015) (Fig. 9b). In contrast, HypoLine applies a linear extension of the $M_L$ relationship (Richter, 1958), empirically calibrated to extremely short distances (<300 m) (Wust-Bloch and Joswig, 2006) (Fig. 9b):

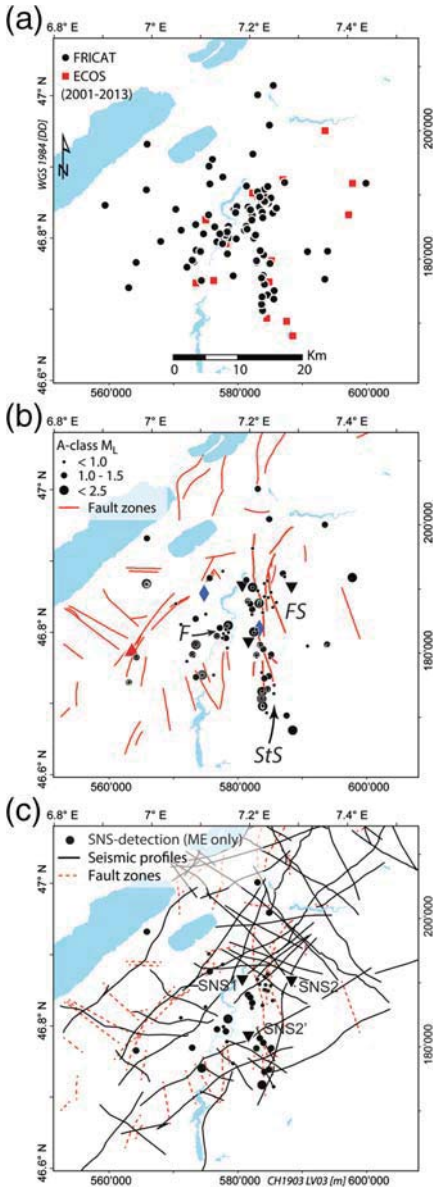


**Figure 8.** (a) Epicenter map of ECOS events (located by HypoLine software, squares) and events newly detected by sonogram analysis (FRICAT, circles). (b) Zones with apparent clustered seismicity are better delineated by the projection of class A epicenters and correlate well to fault zones interpreted by Interoil (2010) in seismic profiles, especially along the St-Sylvester (*StS*) and the Fribourg structures (*FS*). (c) The unmatched events constrained by SNS records illuminate the main seismicity trend in the Fribourg region, revealing the existence of previously undetected tectonic features, where no seismic profiles (bold lines) are available (*F*). The color version of this figure is available only in the electronic edition.

$$M_L = \log_{10}(A_{WA}) + 1 \times \log_{10}(D) + 0.70 - \log_{10}(2.8) \quad \text{for } D \le 3 \text{ km} \tag{1}$$

$$M_L = \log_{10}(A_{WA}) + 1.5 \times \log_{10}(D) + 0.45 - \log_{10}(2.8) \quad \text{for } 3 < D \le 100 \text{ km} \tag{2}$$

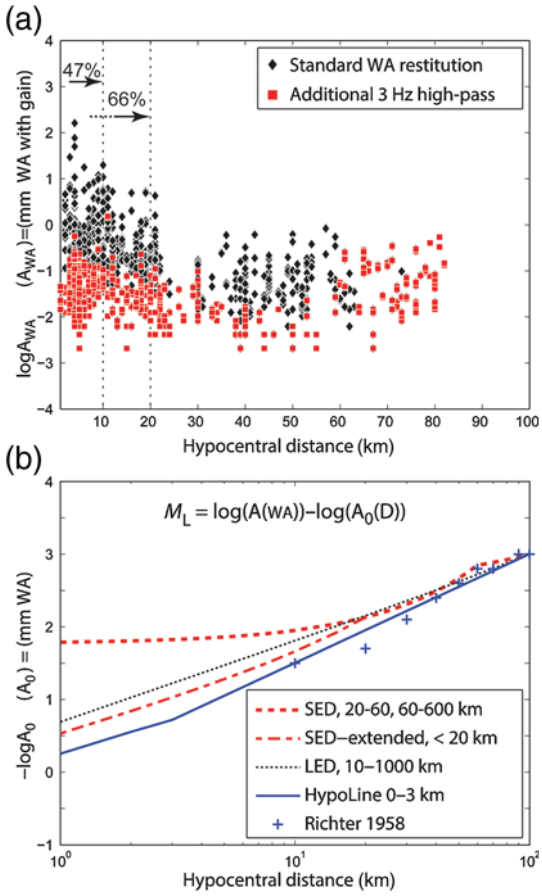


**Figure 9.** (a) Amplitude–distance relationships for 321 FRICAT events (688 A–D pairs) showing that source–receiver distance is below 20 km for 66% of the dataset and below 10 km for 47% of the dataset. Diamonds indicate data with standard Wood–Anderson (WA) restitution (squares) display low-SNR (signal-to-noise ratio) records with additional 3-Hz high pass to the standard WA restitution. (b) Attenuation relationships for local seismicity according to SED (Kradolfer, 1984) and empirically extended below 20 km by Edwards *et al.* (2015) (hatched lines), LED (Stange, 2006) (dotted line), HypoLine (Wust-Bloch and Joswig, 2006) (bold line), and Richter (Richter, 1958) (crosses). Calibrated distance range of each relationship is indicated in the legend. The color version of this figure is available only in the electronic edition.

$$M_L = \log_{10}(A_{WA}) + 2.56 \times \log_{10}(D) - 1.67 - \log_{10}(2.8) \quad \text{for } D > 100 \text{ km}, \tag{3}$$

in which $A_{WA}$ is half of the maximum peak-to-peak amplitude on the dominant horizontal waveform of the simulated Wood–Anderson (WA) traces in micrometers. $D$ is the epicentral distance in kilometers if the epicentral distance is larger than 10 km and the depth larger than half the epicentral distance; otherwise the hypocentral distance is used. The factor $\log_{10}(2.8)$ corrects for the gain of 2800 applied on WA restitution in standard $M_L$ computation procedures (e.g., Kradolfer, 1984; Stange, 2006; Bormann *et al.*, 2012; and see Deichmann, 2011, in Data and Resources) and for the use of amplitudes in micrometers instead of millimeters as is the case for HypoLine's distance–correction curve.

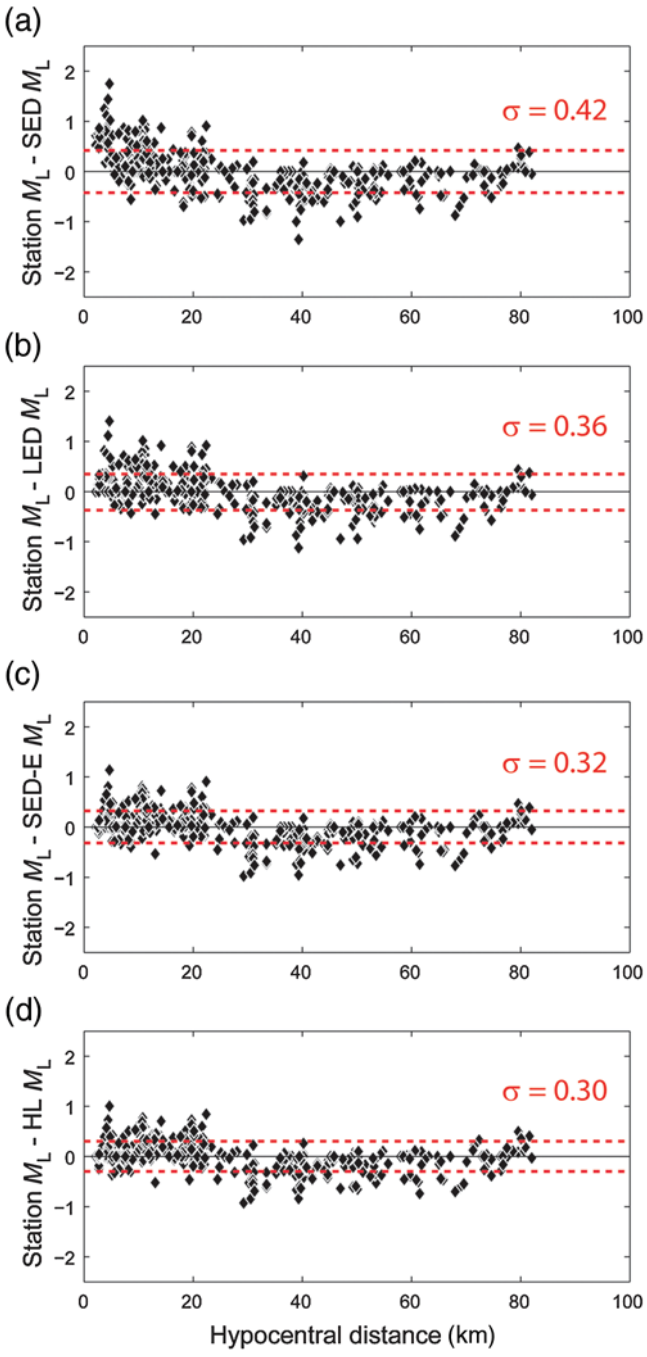


**Figure 10.** Magnitude residuals (station magnitude−event magnitude) with distance for (a) SED (Kradolfer, 1984), (b) LED (Stange, 2006), (c) SED-extended (Edwards *et al.*, 2015), and (d) HypoLine (Wust-Bloch and Joswig 2006) relationships. Dotted lines indicate one standard deviation ($\sigma$). The minimal bias observed with HypoLine relationship justifies its use for FRICAT. The color version of this figure is available only in the electronic edition.

The differences between the station magnitudes and the median magnitude of each event are compared for SED, LED, SED-extended, and HypoLine relationships as a function of hypocentral distance (Fig. 10). A strong bias toward higher magnitudes is introduced at short distances by SED and LED attenuation relationships, empirically calibrated for distances above 10–20 km (Fig. 10a,b). The trend is reduced by the new SED-extended relationship (Edwards *et al.*, 2015), whereby station magnitudes scatter with a standard deviation ($\sigma$) of 0.32 about the median (Fig. 10c), instead of 0.36 for LED and 0.42 for SED relationships. However, the lowest standard deviation (0.30) is returned by the HypoLine relationship (Fig. 10d). The attenuation pattern of amplitudes with distance is compared with SED, LED, SED-extended, and HypoLine relationships for 15 ECOS events ($M_L > 1$) for which amplitudes could be picked in the 5–80 km range (Fig. 11). Because a good match is observed between the slopes pictured by the projections of WA amplitudes with distance and the HypoLine distance-attenuation function, the HypoLine relationship is considered as appropriate for use in a microseismic dataset. HypoLine's relationship is therefore selected to compute the final FRICAT magnitude catalog. Because numerous WA amplitude readings at short distances present significant differences in the north and the east components (see asterisks in Fig. 11), we follow Bormann *et al.* (2012) and compute station local magnitude ($M_{ST}$) as the mean of both independent east- and north-component local magnitudes

$$M_{ST} = \frac{M_{LE} + M_{LN}}{2}. \quad (4)$$

The final $M_L$ is taken as the median value of the station magnitudes. The median, which is less sensitive to outliers, is also used by SED and LED (see Deichmann, 2011, in Data and Resources; Stange, 2006). FRICAT local magnitudes are estimated on the basis of readings at the nine SED stations used in this study (Fig. 1). Amplitudes are not used for data recorded by SNS, because no robust calibration relationship could be found between SNS and SED records. As a result, six events recorded only by SNS are not evaluated for $M_L$. The magnitude catalog includes 688 distance–amplitude pairs for 321 events and ranges over four order of magnitudes: $-1.69 < M_L < 2.42$. Sonogram analysis carried out on existing Swiss seismic records significantly contributed to lower the detection threshold in the target area (Fig. 12a,b). The two SED accelerometers operating since 2009 in the Fribourg area increase ECOS event detection in the 1–2 magnitude range. However, most $M_L < 1$ events remain undetected by SED even after 2009. Because the FRICAT dataset still falls into the statistics of small numbers, no attempt was made to carry out comprehensive estimations of completeness magnitude or *a*- and *b*-value parameters (see Wiemer and Wyss, 2000; Woessner and Wiemer, 2005). Nevertheless, the frequency–magnitude distribution (FMD) (0.1 binned) is estimated in two ways (Fig. 12d). First, the FMD is computed individually for all 304 events (ECOS and sonogram new detections) from March 2009 to April 2013. This FMD gives the magnitude of completeness of the full 2009–2013 dataset with continuous detection by sonogram screening (solid symbols). Second, the FMD is estimated only with higher magnitude ECOS events from 2001–2013 (crosses) to obtain the $M_c$ for the ECOS original catalog. The estimated $M_c$ values for both datasets are indicated

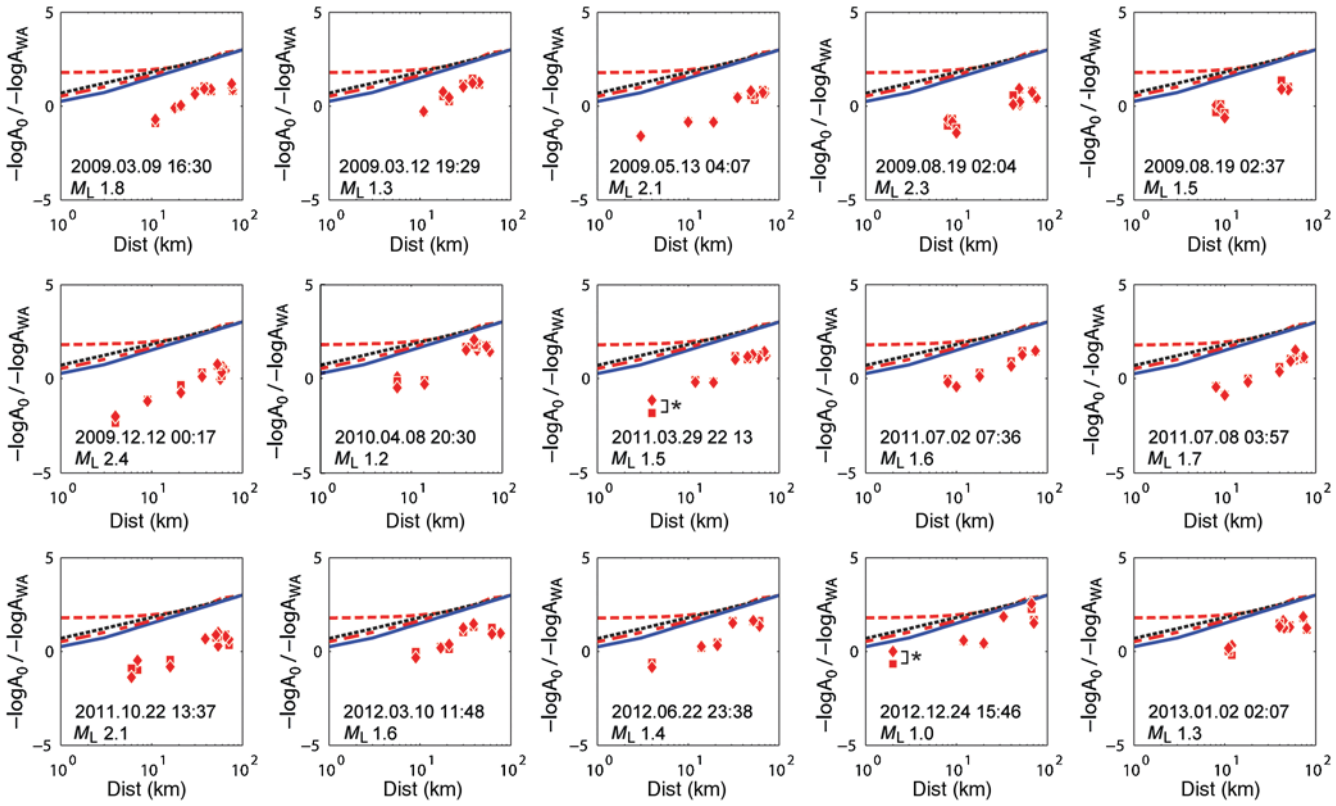


**Figure 11.** The WA amplitudes for east (diamonds) and north (squares) components of Swiss permanent stations in the 5–80 km distance range are compared to SED (Kradolfer, 1984; Edwards *et al.*, 2015) (hatched lines), LED (Stange 2006) (dotted line), and HypoLine (Wust-Bloch and Joswig, 2006) (bold line) distance attenuation relationships for 15 ECOS events. The color version of this figure is available only in the electronic edition.

by dotted lines on the diagram. The result indicates a lowering of $M_c$ by ~0.8. Thus, it can be seen that the sonogram analysis resulted in reducing the original magnitude of completeness ($M_c$) for ECOS dataset by close to one magnitude unit.

## Conclusions

Nanoseismic monitoring, a nonstandard and analyst-guided approach, succeeds in providing a robust analysis of a low-seismicity region while drastically reducing monitoring time. Sonogram analysis of SED records at three stations in the Fribourg area resulted in a factor of 9 increase of earthquake detection relative to the ECOS catalog for the period 2009–2013. The interactive HypoLine location scheme derives epicentral solutions that are consistent with those obtained by standard residual-based NLL (Lomax *et al.*, 2000). The jackknifing graphical approach of HypoLine screens particularly well erroneous phase onsets, making it crucial for processing low-SNR signals for which phase identification is not trivial. The trial-and-error approach of HypoLine is especially suited to the evaluation of weak events with few and minimal-SNR onsets. Our study suggests that it would be optimal to integrate all approaches as follows: (1) sonogram-supported template search for event detection without prior information, (2) sonogram-based template matching filters for detection of repeating events, (3) HypoLine location for initial source parametrization and outlier screening, and (4) advanced NLL for final hypocentral relocation.

This work shows that a better model for local seismicity generated within the Fribourg region can be obtained by advanced array detection and processing over just 3 yrs (2010–2013) rather than by standard methods over 32 yrs (see Fäh *et al.*, 2011, in Data and Resources). Such a significant lowering of the monitoring time illustrates the potential of this novel approach in terms of event detection and location in regions of low seismicity, suboptimal network coverage, and high background seismic noise level. A previously undetected zone of microseismic activity has been resolved below the city of Fribourg where no subsurface imaging data are available. Detecting and analyzing blind fault zones under urban areas is crucial, especially when they are targeted by future induced seismicity operations. The shallow event depths (preferentially within 1–3 km) obtained by HypoLine corroborate well with those constrained by modeling sPMP–PMP travel-time differences on synthetic seismograms for the 1995 earthquake sequence in the Fribourg area (Kastrup *et al.*, 2007). These results suggest that the observed seismicity is restricted to

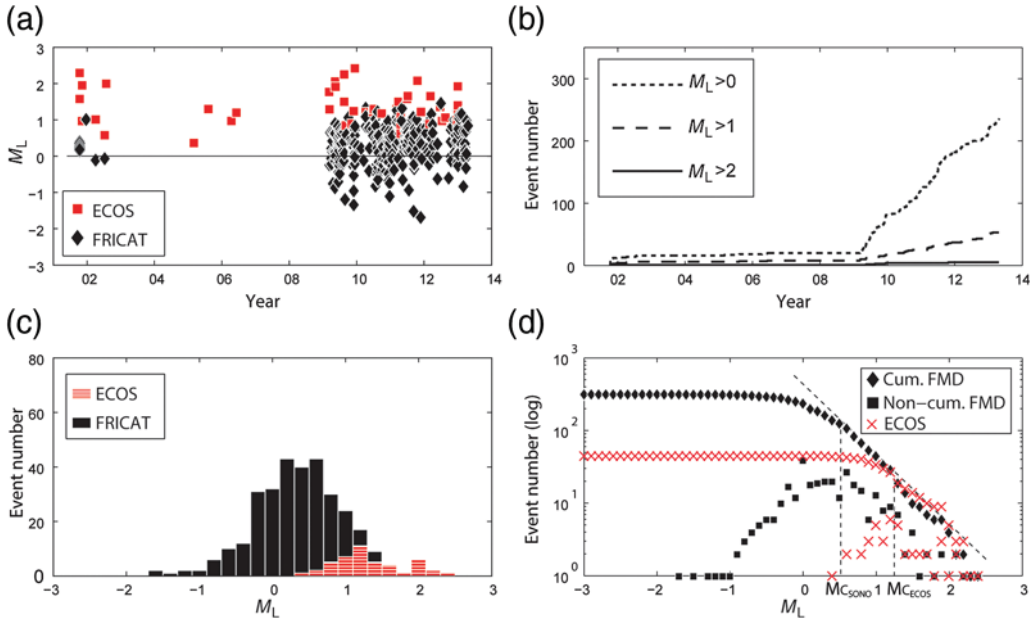


**Figure 12.** Magnitude catalog computed based on HypoLine $M_L$ relationship (Wust-Bloch and Joswig, 2006). (a) Magnitude distribution between October 2001 and April 2013 of ECOS events (squares) and newly detected FRICAT events (diamonds). (b) Cumulative number of ECOS and FRICAT events for the same period. (c) Magnitude distribution (0.2 binned) of ECOS events (striped) and newly detected FRICAT events (solid). (d) Cumulative and noncumulative frequency–magnitude distribution (FMD) (0.1 binned). The $M_c$ estimated for the two datasets is indicated with a dotted line and shows a 0.8 lowering of $M_c$. The color version of this figure is available only in the electronic edition.

the sedimentary cover and occurs along fault zones decoupled from the crystalline basement. The low magnitudes ($M_L$ < 2.4) and short recurrence times observed for the seismicity generated within the Fribourg area seem to fit a model where seismic energy is released over a dense network of small faults (< 100 m). However, because they cluster over a 20-km seismically active zone, they present a significant hazard for the city of Fribourg.

## Data and Resources

The data used for this study integrate two datasets: (1) Swiss Seismological Service (SED) waveforms (http://arclink.ethz.ch/webinterface/, last accessed January 2016); and (2) Seismic Navigating System (SNS) records (March 2010–April 2013), which are stored at Fribourg University. The final FRICAT database as well as codes and documentation are available upon request from the authors. References with regard to the Earthquake Catalogue of Switzerland (ECOS; http://hitseddb.ethz.ch:8080/ecos09/publications.html?&locale=en, last accessed January 2016) include "Appendix H: Swiss instrumental local magnitudes, in ECOS-09 Earthquake Catalogue of Switzerland Release 2011, Report and Database, Public Catalogue, 17.4.2011, 12 pp.," by N. Deichmann and "ECOS-09 Earthquake Catalogue of Switzerland Release 2011, Report and Database, Public catalogue, 17.4.2011," by D. Fäh, D. Giardini, P. Kästli, N. Deichmann, M. Gisler, G. Schwartz-Zanetti, S. Alvare-Rubio, S. Sellami, B. Edwards, B. Allmann, F. Bethmann, J. Woessner, G. Gassner-Stamm, S. Fritsche, and D. Eberhard.

## Acknowledgments

This project was financially supported by the REmplacement SUisse Nucléaire (RESUN AG) and the Bernische Kraftwerke (BKW) (Project Number R49000048 KB). The authors would like to thank Manfred Joswig and Benjamin Sick (Stuttgart University) for providing nanoseismic monitoring expertise; Nicolas Deichmann, Toni Kraft, and Stephan Husen (Swiss Seismological Service [SED], ETH-Zurich) for sharing data, scripts, and insightful comments; Christian Sue (Franche-Comté University) for fruitful discussions; and Christoph Neururer (Fribourg University) for technical and logistical support. The authors also thank Associate Editor Eric Chael and two reviewers, Andreas S. Eisermann and Jean Virieux, for their constructive comments.

## References

Baer, M. (1992). *SNAP, A Seismic Network Analysis Program, XIII*, General Assembly of the European Seismological Commission (ESC), Prague, Czech Republic.

Bormann, P., M. Baumbach, G. Bock, H. Grosser, G. L. Choy, and J. Boatwright (2012). Seismic sources and source parameters, in *New Manual of Seismological Observatory Practice 2 (NMSOP-2)*, P. Bormann (Editor), IASPEI, Potsdam, Germany, 94 pp.

Clinton, J., C. Cauzzi, D. Fäh, C. Michel, P. Zweifel, M. Olivieri, G. Cua, F. Haslinger, and D. Giardini (2011). The current state of strong motion monitoring in Switzerland earthquake data, in *Engineering Seismology: Geotechnical, Geological, and Earthquake Engineering*, S. Akkar, P. Gülkan, and T. van Eck (Editors), Vol. 14, Springer Science + Business Media B.V. 2001, Dordrecht, The Netherlands, 219–233.

Deichmann, N., and D. Giardini (2009). Earthquakes induced by the stimulation of an enhanced geothermal system below Basel (Switzerland), *Seismol. Res. Lett.* **80,** no. 5, 784–798, doi: 10.1785/gssrl.80.5.784.

Deichmann, N., M. Baer, J. Braunmiller, D. Ballarin Dolfin, F. Bay, B. Delouis, D. Fäh, D. Giardini, U. Kastrup, F. Kind, *et al.* (2000). Earthquakes in Switzerland and surrounding regions during 1999, *Eclogae Geol. Helv.* **93,** 395–406.

Deichmann, N., J. Clinton, S. Husen, B. Edwards, F. Haslinger, D. Fäh, D. Giardini, P. Kästli, U. Kradolfer, I. Marschall, *et al.* (2010). Earthquakes in Switzerland and surrounding regions during 2009, *Swiss J. Geosci.* **103,** no. 3, 535–549, doi: 10.1007/s00015-010-0039-8.

Diehl, T., J. Clinton, T. Kraft, S. Husen, K. Plenkers, A. Guilhelm, Y. Behr, C. Cauzzi, K. Kästli, F. Haslinger, *et al.* (2014). Earthquakes in Switzerland and surrounding regions during 2013, *Swiss J. Geosci.* **107,** nos. 2/3, 359–375, doi: 10.1007/s00015-014-0171-y.

Diehl, T., E. Kissling, S. Husen, and F. Aldersons (2009). Consistent phase picking for regional tomography models: Application to the greater Alpine region, *Geophys. J. Int.* **176,** no. 2, 542–554, doi: 10.1111/j.1365-246X.2008.03985.x.

Edwards, B., T. Kraft, C. Cauzzi, P. Kastli, and S. Wiemer (2015). Seismic monitoring and analysis of deep geothermal projects in St Gallen and Basel, Switzerland, *Geophys. J. Int.* **201,** no. 2, 1022–1039, doi: 10.1093/gji/ggv059.

Eisermann, A. S., A. Ziv, and G. H. Wust-Bloch (2015). Real-time back azimuth for earthquake early warning, *Bull. Seismol. Soc. Am.* **105,** no. 4, 2274–2285, doi: 10.1785/0120140298.

Fäh, D., D. Giardini, F. Bay, F. Bernardi, J. Braunmiller, N. Deichmann, M. Furrer, L. Gantner, M. Gisler, D. Isenegger, *et al.* (2003). Earthquake Catalogue of Switzerland (ECOS) and the related macroseismic database, *Eclogae Geol. Helv.* **96,** 219–236.

Gibbons, S. J., and F. Ringdal (2006). The detection of low magnitude seismic events using array-based waveform correlation, *Geophys. J. Int.* **165,** 149–166, doi: 10.1111/j.1365-246X.2006.02865.x.

Häge, M., P. Blascheck, and M. Joswig (2013). EGS hydraulic stimulation monitoring by surface arrays—Location accuracy and completeness magnitude: The Basel Deep Heat Mining Project case study, *J. Seismol.* **17,** no. 1, 51–61, doi: 10.1007/s10950-012-9312-9.

Husen, S., E. Kissling, N. Deichmann, S. Wiemer, D. Giardini, and M. Baer (2003). Probabilistic earthquake location in complex three-dimensional velocity models: Application to Switzerland, *J. Geophys. Res.* **108,** no. B2, doi: 10.1029/2002JB001778.

Interoil (2010). 2D seismic interpretation in den Gebieten Payerne, Fribourg und Berner Seeland, *Bericht vorbereitet von Interoil E&P Switzerland AG für die RESUN AG*, Zürich, Switzerland, 28 pp. (in German).

Joswig, M. (1990). Pattern recognition for earthquake detection, *Bull. Seismol. Soc. Am.* **80,** 170–186.

Joswig, M. (1995). Automated classification of local earthquake data in the BUG small array, *Geophys. J. Int.* **120,** 262–286.

Joswig, M. (2008). Nanoseismic monitoring fills the gap between microseismic networks and passive seismic, *First Break* **26,** 117–124.

Kastrup, U., N. Deichmann, A. Fröhlich, and D. Giardini (2007). Evidence for an active fault below the northwestern Alpine foreland of Switzerland, *Geophys. J. Int.* **169,** no. 3, 1273–1288, doi: 10.1111/j.1365-246X.2007.03413.x.

Kradolfer, U. (1984). Magnitudenkalibrierung von Erdbebenstationen in der Schweiz, *Diplomarbeit*, ETHZ, Zürich, Switzerland, 100 pp. (in German).

Kraft, T., P. M. Mai, S. Wiemer, N. Deichmann, J. Ripperger, P. Kästli, C. Bachmann, D. Fäh, J. Wössner, and D. Giardini (2009). Enhanced geothermal systems: Mitigating risk in urban areas, *Eos Trans. AGU* **90,** no. 32, 273–280.

Kraft, T., A. Mignan, and D. Giardini (2013). Optimization of a large-scale microseismic monitoring network in northern Switzerland, *Geophys. J. Int.* **195,** no. 1, 474–490, doi: 10.1093/gji/ggt225.

Lomax, A., A. Michelini, and A. Curtis (2009). Earthquake location, direct, global-search methods, in *Encyclopedia of Complexity and Systems Science*, R. Meyers (Editor), Springer, New York, New York, 2449–2473.

Lomax, A., J. Virieux, P. Volant, and C. Berge-Thierry (2000). Probabilistic earthquake location in 3D and layered models: Introduction of a Metropolis–Gibbs method and comparison with linear locations, in *Advances in Seismic Event Location*, N. Rabinowitz and C. H. Thurber (Editor), Kluwer, Amsterdam, The Netherlands, 101–134.

Meier, B. P. (2010). Ergänzende Interpretation reflexionsseismischer Linien zwischen dem östlichen und westlichen Molassebecken—Gebiete Waadtland Nord, Fribourg, Berner Seeland und Jurasüdfuss zwischen Biel und Oensingen, *Nagra Interner Bericht*, NIB 09–09 (in German).

Nanjo, K. Z., D. Schorlemmer, J. Woessner, S. Wiemer, and D. Giardini (2010). Earthquake detection capability of the Swiss Seismic Network, *Geophys. J. Int.* **181,** 1713–1724, doi: 10.1111/j.1365-246X.2010.04593.x.

Plenkers, K., J. R. R. Ritter, and M. Schindler (2013). Low signal-to-noise event detection based on waveform stacking and cross-correlation: Application to a stimulation experiment, *J. Seismol.* **17,** 27–49, doi: 10.1007/s10950-012-9284-9.

Richter, C. F. (1958). *Elementary Seismology*, W. H. Freeman and Co., San Fransisco, California.

Schaff, D. P., and F. Waldhauser (2010). One magnitude unit reduction in detection threshold by cross-correlation applied to Parkfield (California) and China seismicity, *Bull. Seismol. Soc. Am.* **100,** no. 6, 3224–3238, doi: 10.1785/0120100042.

Sick, B., M. Guggenmos, and M. Joswig (2015). Chances and limits of single-station seismic event clustering by unsupervised pattern recognition, *Geophys. J. Int.* **201,** 1801–1813, doi: 10.1093/gji/ggv126.

Sick, B., M. Walter, and M. Joswig (2012). Visual event screening of continuous seismic data by supersonograms, *Pure Appl. Geophys.* **171,** no. 3, 549–559, doi: 10.1007/s00024-012-0618-x.

Stange, S. (2006). $M_L$ determination for local and regional events using a sparse network in southwestern Germany, *J. Seismol.* **10,** no. 2, 247–257, doi: 10.1007/s10950-006-9010-6.

Trnkoczy, A. (2012). Understanding and parameter setting of STA/LTA trigger algorithm: IS 8.1, in *New Manual of Seismological Observatory Practice 2 (NMSOP-2)*, P. Bormann (Editor), IASPEI, Potsdam, Germany, 1–20.

Vouillamoz, N. (2015). *Microseismic Characterization of Fribourg area (Switzerland) by Nanoseismic Monitoring*, *Thesis, GeoFocus*, Vol. 38, University of Fribourg, Switzerland, 274 pp, ISSN: 1424-1463.

Wiemer, S., and M. Wyss (2000). Minimum magnitude of completeness in earthquake catalogs: Examples from Alaska, the western United States, and Japan, *Bull. Seismol. Soc. Am.* **90,** no. 4, 859–869.

Withers, M., R. Aster, C. Young, J. Beiriger, M. Harris, S. Moore, and J. Trujillo (1998). A comparison of selected trigger algorithms for automated global seismic phase and event detection, *Bull. Seismol. Soc. Am.* **88,** no. 1, 95–106.

Woessner, J., and S. Wiemer (2005). Assessing the quality of earthquake catalogues: Estimating the magnitude of completeness and its uncertainty, *Bull. Seismol. Soc. Am.* **95,** no 2, 684–698, doi: 10.1785/0120040007.

Wust-Bloch, G. H., and M. Joswig (2006). Pre-collapse identification of sinkholes in unconsolidated media at Dead Sea area by 'nanoseismic monitoring' (graphical jackknife location of weak sources by few, low-SNR records), *Geophys. J. Int.* **167,** no. 3, 1220–1232, doi: 10.1111/j.1365-246X.2006.03083.x.

Department of Geosciences
University of Fribourg
6, Chemin du Musée
1700 Fribourg, Switzerland
naomi.vouillamoz@unifr.ch
martinussatiapurwadi.abednego@unifr.ch
jon.mosar@unifr.ch
(N.V., M.A., J.M.)

Department of Geophysics and Planetary Sciences
Tel Aviv University
P.O. Box 39040
Tel Aviv 69978, Israel
hillelw@tau.ac.il
(G.H.W.-B.)